Levitation of evaporating microscale droplets over solid surfaces

Vladimir S. Ajaev
Department of Mathematics, Southern Methodist University, Dallas, Texas 75275, USA

Dmitry V. Zaitsev and Oleg A. Kabov
Institute of Thermophysics, SB RAS, Novosibirsk 630090, Russia
and Novosibirsk State University, Novosibirsk 630090, Russia

(Received 23 August 2020; accepted 19 April 2021; published 20 May 2021)

We develop an analytical model to describe recent experimental observations of levitation of evaporating microscale droplets over heated solid surfaces at temperatures far below the Leidenfrost point. Viscous flow patterns around the droplet are determined from the solution of the equation for the Stokes stream function in bipolar coordinates. The results are compared to the predictions of models representing microscale droplets as point sources in the Stokes flow equations. Formulas for the force acting on the droplet as a result of moist air flow around it are derived and used to obtain predictions of levitation height as a function of droplet size which are in very good agreement with the experimental data. In addition to gravity, three physical mechanisms are identified which contribute to the force acting on the droplet: repulsive interaction of the droplet with the solid, spatially nonuniform evaporation along the liquid surface, and thermocapillary effect. The first two act against gravity and allow droplets to levitate despite competing thermocapillary stresses which push the moist air out of the region between the droplet and the solid. Relative importance of the three mechanisms is evaluated based on an analytical model of heat transfer both inside and outside of the droplet.

DOI: 10.1103/PhysRevFluids.6.053602

I. INTRODUCTION

Models of evaporating droplets are important for a wide range of applications such as spray cooling, internal combustion engines, and aerosol drug delivery [1–3]. Droplet sizes in many of these applications are well below the capillary length of the liquid (about 2.7 mm for water), so the free surface shapes, dominated by the capillary forces, are nearly spherical. This offers advantages for mathematical modeling, as Maxwell [4] first demonstrated by using a steady diffusion equation to describe spherically symmetric distribution of vapor around the droplet. The balance between evaporative mass loss and the diffusion flux away from the droplet in this framework leads to the classical D^2 law, i.e., the conclusion that the square of the droplet diameter will decrease as a linear function of time, a trend indeed observed in many experimental studies [5].

Predictions of diffusion-based evaporation models can strongly deviate from the experimental data due to convective flow in the gas around the droplet. The flow can be caused by factors not related to the presence of the droplet, e.g., natural convection, or generated by the droplet itself. The latter has to do with the fact that, even in spherically symmetric geometry, mass transfer around the droplet is not purely diffusive, as was first pointed out in the classical works of Stefan [6] and Fuchs [7]. The following simple argument [5] illustrates the origin of convective mass transfer known as Stefan flow. Suppose gradient of partial density of vapor in the moist air is established as a result of evaporation from the droplet surface. Assuming the total density of the gas phase to

be constant, there also has to be gradient, in the opposite direction, of the partial density of the remaining components of air, i.e., nitrogen, oxygen, etc. Thus these components are transported towards the free surface. However, since these gas molecules do not penetrate the free surface, flow has to develop to ensure the global mass conservation condition. The effect becomes stronger as the evaporation intensity increases. Over the past several decades, a number of modeling studies and numerical simulations of evaporating droplets and Stefan flow were conducted, reviewed by, e.g., Sirignano [2] and Sazhin [5].

When an evaporating droplet ends up in the vicinity of a solid surface, the evaporation can lead to a repulsive force. The most dramatic demonstration of this effect is the well-known Leidenfrost phenomenon [8,9]. While originally observed for macroscale droplets, more recently the Leidenfrost effect was studied extensively for microscale droplets as well, typically the ones formed from larger droplets as a result of gradual mass loss by evaporation. A number of novel phenomena such as sudden droplet takeoff and explosive breakup at sufficiently small size were observed and explained [10,11]. However, it is important to emphasize that all studies of the Leidenfrost effect consider relatively high temperatures, far above the boiling point of liquid.

Recent experiments conducted in our group illustrated that the mechanism of repulsion of evaporating droplets from solid surfaces is operational and can lead to levitation at temperatures far below the Leidenfrost point and even below the boiling temperature of the liquid [12–14]. It was established in previous studies that small droplets of condensate can form and levitate over the surfaces of evaporating liquid layers [15,16]. This phenomenon is similar to formation of a layer of fine mist over a cup of tea or coffee [17]. While in all these previous studies droplets were levitating near the free surface of liquid, Zaitsev *et al.* [13] created a dry patch in the evaporating layer and focused on the behavior of the condensate droplets which ended up over the dry patch rather than near the surface of the liquid layer. Remarkably, these droplets were levitating as well until they completely evaporated. To explain the phenomenon, a mathematical model was developed which treats levitating droplets as point sources. The model is shown to agree with experiments for droplets of small sizes, but failed to describe experimental trends for larger droplets. The present study will address the effect of finite droplet size on the levitation conditions. The flow around the droplet will be described, in the Stokes flow approximation, using an analytical approach based on bipolar coordinates.

An important outcome of our study is a formula for the force acting on the droplet, a useful result for applications, some of which are not directly related to levitation. In fact, a levitating droplet is a unique tool for studies of repulsive interaction between droplets and flat interfaces. Since the droplet is at rest, its weight, easily estimated from the image analysis, is equal to the force that repels it from the interface. Such force is important to know in a number of applications. For example, in spray cooling [1], repulsion of droplets from a heated surface can result in dramatic decrease of heat transfer efficiency. In the commonly used drug delivery method by aerosol inhalation, the microscale aqueous droplets are carried by the air flow into pulmonary airways [3]. The location of droplet deposition at the walls of the airways is a key parameter determining the success of the therapy and that location can change due to repulsive droplet-wall interaction typically not accounted for in the numerical models.

Stokes flow around a spherical droplet in the presence of another droplet or near a flat interface has been described analytically using bipolar coordinates in a number of well-known studies [18–20]. The governing equations are reformulated in terms of the Stokes stream function, leading to a single equation which is then solved using the method of separation of variables. The technique has been adopted to situations when evaporation is taking place at the liquid-gas interfaces [21,22]. In particular, interaction of two evaporating spherical droplets was investigated by Oguz *et al.* [22]. They imposed uniform evaporation velocities at liquid-gas interfaces and thus did not have to model heat transfer in order to describe droplet interaction. More elaborate models of the two-droplet configuration with evaporation [23], based on earlier pioneering studies from combustion literature [24,25], account for heat transfer both inside and outside of the droplets.

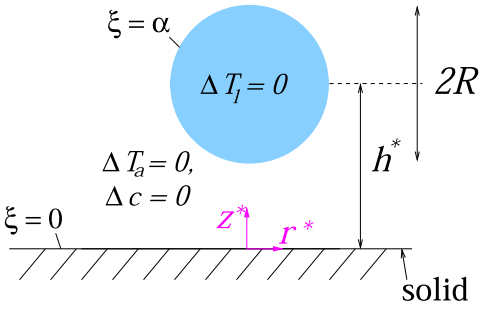

FIG. 1. Sketch of the geometric configuration—an evaporating spherical droplet of radius R near a heated solid surface. Dimensional cylindrical coordinates (r^*, z^*) are shown in the sketch and governing equations for heat transfer in liquid and air are specified. Vapor diffusion in air is coupled to the thermal problem via conditions at the droplet surface.

Zhang and Gogos [26] used bipolar coordinates to investigate evaporation of droplets near hot surfaces under conditions motivated by experimental studies of the Leidenfrost phenomenon so that evaporation rate is high and the temperatures are typically above 500 K. In the present study, we apply this general framework to droplet evaporation at moderate temperatures [13]. Our study is different from Zhang and Gogos [26] in the following four aspects. First, the moderate temperature values allow us to identify the limit of small vapor concentration leading to dramatic simplification of the model. Second, we investigate the effect of Marangoni stresses on the flow around the droplet. Third, we consider a droplet in an imposed external temperature gradient rather than using the condition of constant temperature away from the droplet. Finally, while the work of Zhang and Gogos [26] was purely theoretical, we provide direct comparison of our results to experimental data.

The paper is organized as follows. In Sec. II, we discuss the geometric configuration and the heat transfer model for both inside and outside of the droplet, coupled to the steady diffusion equation for vapor concentration in air. Due to small values of the Péclet number, the governing equations for heat transfer are decoupled from the fluid flow description. Once temperature and evaporative mass flux are found on the droplet surface, the fluid flow problem can be solved using the Stokes flow approximation, the subject of Sec. III. Flow patterns found from the solution of the flow equations are described in Sec. IV, followed by the calculation of the force acting on the droplet in Sec. V. Thermocapillary effects are discussed in Sec. VI. Predictions of the model are compared to the experimental data in Sec. VII. Finally, conclusions are presented in Sec. VIII.

II. PROBLEM GEOMETRY AND HEAT TRANSFER MODEL

Consider a spherical droplet of radius R evaporating near a heated solid surface, as sketched in Fig. 1. The dimensional cylindrical coordinates (r^*, z^*) are also shown in the sketch, with the z^* axis coinciding with the axis of symmetry of the configuration. Levitation height, i.e., the distance between the center of the droplet and the solid, is denoted by h^*. In experiments, typical values of the droplet levitation height are below 30 μm, i.e., the droplets are very close to the heater [13]. The droplet radii are initially near 15 μm but gradually decay as a result of evaporation at a rate $\dot{R} \sim 5$ μm/s. Conservation of mass then suggests the value of moist air velocity near droplet surface $V^* = \dot{R}\hat{\rho}$, with $\hat{\rho}$ denoting the liquid-to-air density ratio. The significance of convective heat transfer is measured by the Péclet number, $\mathrm{Pe} = RV^*/\kappa$, where κ is the thermal diffusivity of moist air. Using $\hat{\rho} = 1.24 \times 10^3$ and $\kappa = 2.30 \times 10^{-5}$ m^2/s, based on moist air properties at 85 °C [27], we estimate the maximum Péclet number to be 4×10^{-3}. The droplet radii would have to be about 3.7 mm for the Péclet number to reach unity under the conditions of experiment of Zaitsev *et al.* [13]. Thus, in our modeling, we will neglect all contributions from convective heat transfer and

write the governing equations for the temperatures in the liquid (T_l) and air (T_a), both scaled by the heated solid surface temperature T_H, as

$$\Delta T_l = 0, \quad \Delta T_a = 0. \tag{1}$$

The length variables r and z in the present section are nondimensionalized by R. Vapor concentration c, scaled by the equilibrium saturation concentration at the temperature T_H, is also described by the Laplace's equation,

$$\Delta c = 0, \tag{2}$$

since the diffusion coefficient of vapor is of the same order of magnitude as thermal diffusivity of moist air and thus the corresponding Péclet numbers for mass transport are small as well.

We follow numerous previous studies [18,20,22,26] and define bipolar coordinates (ξ, η) related to the cylindrical ones via

$$r^* = \frac{R \sinh\alpha \sin\eta}{\cosh\xi - \cos\eta}, \quad z^* = \frac{R \sinh\alpha \sinh\xi}{\cosh\xi - \cos\eta}, \tag{3}$$

where $\alpha = \cosh^{-1}(h^*/R)$. With these choices, the surface of the sphere in Fig. 1 corresponds to $\xi = \alpha$, while the solid is at $\xi = 0$. The boundary conditions at the heated solid surface are formulated as

$$T_a|_{\xi=0} = 1, \tag{4}$$

$$\left.\frac{\partial c}{\partial \xi}\right|_{\xi=0} = 0. \tag{5}$$

At the droplet surface, the temperature is continuous and equilibrium vapor concentration is assumed to be a linear function of the scaled interfacial temperature T_i, leading to the nondimensional boundary conditions

$$T_a|_{\xi=\alpha} = T_l|_{\xi=\alpha} = T_i, \tag{6}$$

$$c|_{\xi=\alpha} = 1 + \gamma(T_i - 1), \tag{7}$$

with $\gamma = \gamma^* T_H/\rho_{\text{sat}}$, γ^* being the rate of change of the dimensional equilibrium vapor saturation density in air with temperature, and ρ_{sat} the value of this density at the temperature T_H. We assume the linear relationship given by (7) to be valid for a sufficiently wide range of temperatures so that γ^* and ρ_{sat} can be evaluated at the reference temperature T_H instead of the actual interfacial temperature. Concentration and temperature gradients are related through the energy balance at the interface, expressed as

$$E\left(1 - \frac{\rho_{\text{sat}}}{\rho}c\right)\left(k\frac{\partial T_a}{\partial \xi} - \frac{\partial T_l}{\partial \xi}\right) = -\frac{\partial c}{\partial \xi}, \tag{8}$$

where the evaporation parameter E is related to the latent heat of phase change $\mathcal{L}$ and vapor diffusion coefficient in air D via

$$E = \frac{k_l T_H}{\mathcal{L} D \rho_{\text{sat}}}, \tag{9}$$

$k = k_a/k_l$, k_i denotes thermal conductivity of air ($i = a$) and liquid ($i = l$), respectively, and ρ is the moist air density. Apart from differences in notation, Eq. (8) is equivalent to the condition used by Zhang and Gogos [26] in their model of Leidenfrost droplets. However, at moderate temperatures well below the Leidenfrost point, vapor saturation density is a small fraction of the total moist air density and Eq. (8) simplifies to

$$E\left(k\frac{\partial T_a}{\partial \xi} - \frac{\partial T_l}{\partial \xi}\right) = -\frac{\partial c}{\partial \xi}. \tag{10}$$

Finally, we assume that far above the droplet, the concentration is a constant value denoted by c_∞ and air temperature approaches a linear profile with specified gradient,

$$T_a = 1 - Gz. \tag{11}$$

Thus an imposed constant temperature gradient is assumed throughout the zone of the experiment. This may appear to contradict the expectation that an unsteady heat conduction model would be more appropriate to describe heat exchange between the metal heater, switched on at the start of the experiment ($t^* = 0$) and generating heat at a constant rate thereafter, and stationary air which is initially at room temperature [13]. Indeed, there is a classical solution of the 1D heat equation for this configuration [28], which predicts the dimensional heat flux q in the air to be

$$q(z^*) = q(0)\left(1 - \mathrm{erf}\frac{z^*}{2\sqrt{\kappa t^*}}\right). \tag{12}$$

In experiments, the heater is turned on for a few minutes before the measurements. Using $t^* \sim 10^2$ s and $z^* \sim 10^{-4}$ m, a value of about an order of magnitude larger than the levitation height, leads to the conclusion that the error function term in the equation is $\sim 10^{-3}$ and thus the imposed temperature gradient can be assumed constant in the region considered in the model. The simplified argument presented here is only valid since the droplets are close to the solid surface and is not meant to rule out unsteady and convective effects in heat transfer in air far above the dry patch over which the droplets are levitating. Based on measured dimensional values of $|dT^*/dz^*|$ on the order of 10 K/mm in experiments with a configuration similar to the one of interest for the present study [29], the values of the parameter $G = R|dT^*/dz^*|/T_H$ in Eq. (11) are $\sim 10^{-4}$. This small value could be set to zero, leading to the standard constant far-field temperature condition used in several previous studies of both droplets and bubbles near heated solid walls [26,30]. However, we feel that it is appropriate to use the nonzero gradient since in experiment heat is continuously generated in the metal substrate and at least part of it is removed through air, suggesting a vertical temperature gradient there.

Following the general approach of the pioneering studies of Zhang and Gogos [26] and Fisher and Golovin [20], we write

$$T_a = 1 - \frac{G\sinh\alpha\,\sinh\xi}{\cosh\xi - \cos\eta} + \sqrt{\cosh\xi - \cos\eta}\sum_{n=0}^{\infty} A_n \sinh\left[\left(n+\frac{1}{2}\right)\xi\right] P_n(\cos\eta), \tag{13}$$

$$T_l = \sqrt{\cosh\xi - \cos\eta}\sum_{n=0}^{\infty} B_n e^{-(n+\frac{1}{2})\xi} P_n(\cos\eta), \tag{14}$$

where P_n denotes the Legendre polynomial of degree n. The terms proportional to $\cosh(n+\frac{1}{2})\xi$ in the expansion for T_a are not included since they contradict the condition from Eq. (4). Also, since T_l is assumed bounded inside the droplet (including the point corresponding to $\xi \to \infty$), only decaying exponentials are included in the expansion for T_l.

The solution for vapor concentration c is expressed in the same coordinate system as

$$c = c_\infty + \sqrt{\cosh\xi - \cos\eta}\sum_{n=0}^{\infty}\left\{C_n \sinh\left[\left(n+\frac{1}{2}\right)(\xi-\alpha)\right] + D_n \cosh\left[\left(n+\frac{1}{2}\right)(\xi-\alpha)\right]\right\} P_n(\cos\eta). \tag{15}$$

Application of the boundary conditions (5) and (7) allows us to express the concentration in terms of the expansion coefficients B_n from Eq. (14) as follows:

$$c = c_\infty + \sqrt{\cosh\xi - \cos\eta}\sum_{n=0}^{\infty}\left\{\tanh\left[\left(n+\frac{1}{2}\right)\alpha\right]\sinh\left[\left(n+\frac{1}{2}\right)(\xi-\alpha)\right] + \cosh\left[\left(n+\frac{1}{2}\right)(\xi-\alpha)\right]\right\}(\sqrt{2}\tilde{c}+\gamma B_n)e^{-(n+\frac{1}{2})\alpha}P_n(\cos\eta), \tag{16}$$

where $\tilde{c} = 1 - c_\infty - \gamma$. In deriving this expression we used an identity that follows directly from the expansion of the generating function for Legendre polynomials [31],

$$(\cosh\alpha - \cos\eta)^{-1/2} = \sqrt{2}\sum_{n=0}^{\infty} e^{-(n+\frac{1}{2})\alpha}P_n(\cos\eta). \tag{17}$$

The coefficients B_n are in turn expressed in terms of A_n using Eq. (6) as

$$B_n = \sqrt{2} - \sqrt{2}(2n+1)G\,\sinh\alpha + A_n e^{(n+\frac{1}{2})\alpha}\sinh\left(n+\frac{1}{2}\right)\alpha. \tag{18}$$

Assuming the temperature to be sufficiently low so that $\rho_{\text{sat}} \ll \rho$, Eq. (10) can now be used to derive a linear system of equations for the coefficients A_n. The result is shown in the Appendix. Solving this system in MATLAB, we obtained the temperature distributions for T_a and T_l in terms of nondimensional coordinates $(r, z) = (r^*/R, z^*/R)$. Figure 2 (top) illustrates a typical solution for parameter values (listed in the caption) based on the physical properties of moist air at 50 °C found from Tsilingiris [27]. We plot the distribution of rescaled temperature $\hat{T}$ defined by

$$\hat{T} = \frac{T - T_0}{1 - T_0}, \tag{19}$$

where T_0 is the temperature (scaled by T_H) at the coldest point of the free surface, which according to our solutions is at the top of the droplet. The value of G is found based on the temperature gradient of ~10 K/mm, while $c_\infty = 0.95$ reflects the fact that the observed evaporation rate of droplets is relatively slow [13], most likely due to the fact that vapor concentration in the region where droplets are observed in experiments is much higher than in the ambient air. This is consistent with the observations of vapor filling the region above the dry patch as a result of intense evaporation from the surrounding liquid layer [12]. Specifically, we estimated the value of the far-field concentration, which was not measured experimentally, by first finding the solution in terms of c_∞ and then adjusting its value iteratively until the rate of mass loss matches the experimentally measured value.

Let us now discuss the physical interpretation of the result shown in Fig. 2 (top). Away from the droplet (near $r = 6$ in the plot) the temperature slowly decays away from the solid surface (located at $z = 0$) as dictated by the imposed temperature gradient G. It is immediately obvious that the presence of the droplet leads to significant perturbation of the temperature field near the heater creating a region of reduced temperature as compared to the profile without the droplet. Note that the results are quasisteady, so the lower temperature of the droplet compared to its surroundings is not a result of the droplet not having enough time to heat through. We believe the result can be explained by a combination of two physical effects. The first one is evaporative cooling: as the liquid evaporates, energy has to be supplied from the outside to maintain evaporation and thus a temperature gradient is established. The second effect, also seen in models of nonevaporating droplets [20], has to do with the droplet thermal conductivity being much larger than that of the surrounding air leading to drastic reduction of temperature gradient through the droplet compared to the imposed gradient.

The plot in Fig. 2 (top) may suggest that the droplet is at uniform temperature, but in reality the bottom of the droplet facing the hot solid surface is still at a higher temperature than the top, as illustrated in Fig. 2 (bottom). Temperature variation across the droplet is higher when the droplet

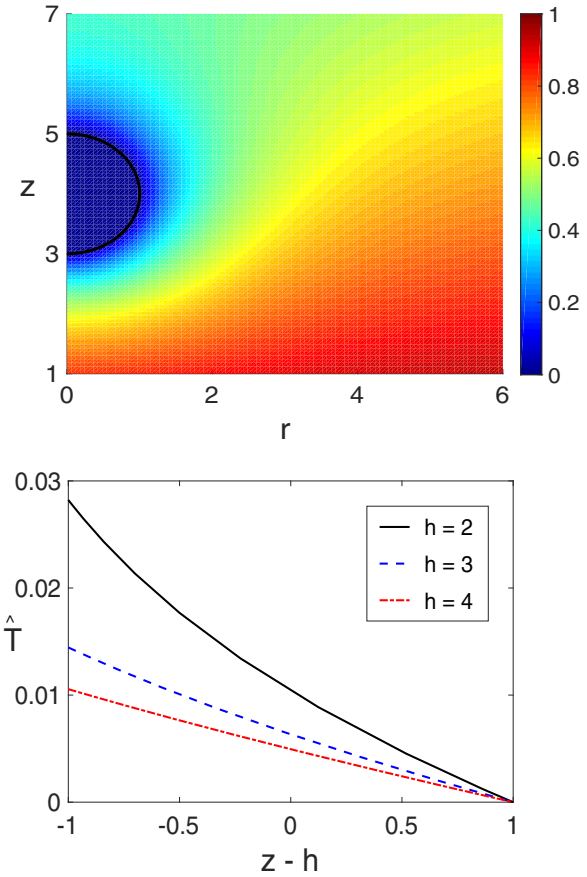

FIG. 2. (Top) Nondimensional temperature distribution both inside and outside of the droplet for $k = 0.042$, $E = 36.1$, and $\gamma = 15.6$. The liquid-gas interface location is shown by the thick black line, the temperature distributions are axially symmetric, and half of the cross section is shown. (Bottom) Droplet surface temperature as a function of the vertical coordinate measured from the position of the center of the droplet, presented in nondimensional variables.

is closer to the hot solid (smaller h), but for all cases the temperature gradient in the liquid is at least an order of magnitude lower than the imposed gradient. That has important implications for shear stresses at the droplet surface due to temperature variation along the interface, i.e., Marangoni stresses, which can be drastically overestimated if the imposed temperature gradient is used to find the temperature variation.

Once the coefficients B_n are found, Eq. (16) can be used to determine vapor concentration distribution and thus calculate the nondimensional evaporative mass flux at the droplet surface, $J \equiv -\partial c/\partial n$. In order to illustrate the degree of nonuniformity of the profile across the droplet, we subtract the value J_0 corresponding to the center of the droplet and plot the result in Fig. 3 for three different droplet locations. Note that the negative values of J do not correspond to condensation but rather indicate values smaller than J_0. The result for $h = 2$ (solid line) may appear counterintuitive since it shows a decrease in the evaporation rate near the bottom of the droplet, despite the fact that this part of the free surface faces the hot surface. We believe the observation can be explained by geometric confinement: as the droplet gets closer to the solid surface, diffusion of vapor away from the free surface is impeded by the presence of the solid, resulting in slower evaporation. This explanation is supported by the fact that J at the bottom of the droplet increases relative to J_0 as

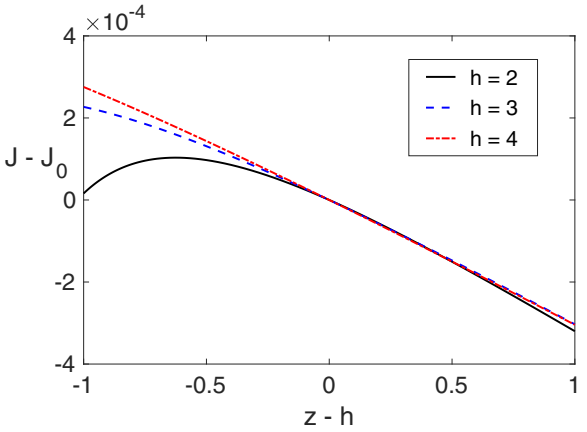

FIG. 3. Scaled evaporation rates along the surface of the droplet plotted in terms of scaled vertical coordinate for different locations of the droplet, measured from $z = h$. The parameter values are the same as in Fig. 2.

the droplet moves away from the solid (dashed and dot-dashed lines in Fig. 3). In fact, the profile is basically linear at $h = 4$ and higher values of h (not shown), i.e., when the droplet is sufficiently far away from the solid. A higher evaporation rate at the bottom and lower rate at the top are dictated there by the imposed temperature gradient.

The results presented so far are valid for relatively low heater temperature since the saturation vapor density has to be a fraction of the moist air density to justify the use of Eq. (10). For the solid surface temperatures in the range between 80 °C and 100 °C, in which many experiments were conducted, Eq. (8) should be used instead. This makes the problem nonlinear, but only at the final step of the solution when the series expansions for temperature and concentration are substituted into Eq. (8). We have carried out this final step of the solution using `fsolve` from MATLAB Optimization Toolbox with a typical result illustrated in Fig. 4. The parameter values are calculated based on $T_H = 85$ °C and the value of c_∞ is adjusted to match the measured evaporation

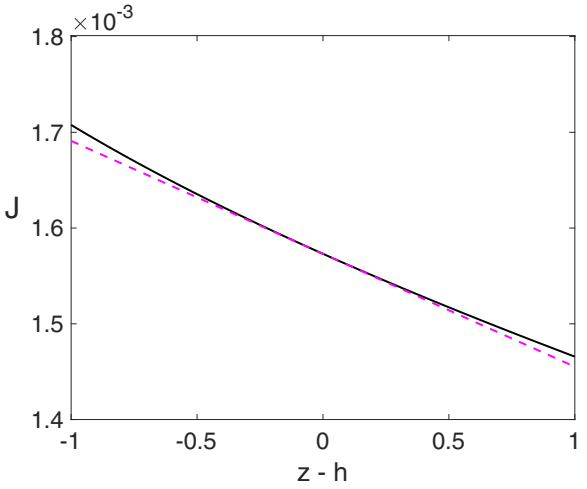

FIG. 4. Scaled evaporation rate plot for $k = 0.04$, $E = 8.53$, $\gamma = 13.3$, and $c_\infty = 0.90$ found based on Eq. (8), solid line. A linear approximation to the profile is shown by the dashed line.

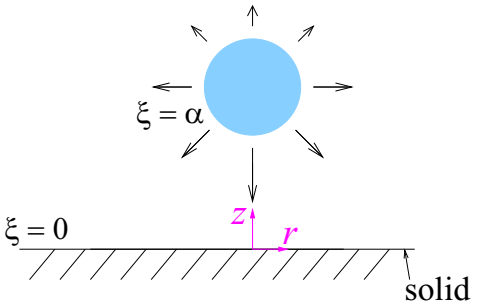

FIG. 5. Sketch illustrating nondimensional coordinates and geometry for the fluid flow model, with arrows schematically showing the direction of the flow away from the droplet surface, with stronger evaporation near the bottom. Stokes flow model is used to describe flow in the gas phase, while internal circulation is neglected due to very low values of the air-to-liquid viscosity ratio.

rate in [13]. Remarkably, the solution is still well approximated by a linear function, which is shown by magenta dashed line in Fig. 4. The slope of this line, defined by the derivative of J at $z = h$, is used in the next section to find the evaporation velocity profile.

III. FLUID FLOW MODEL

Let us now turn to the mathematical description of the flow around a spherical droplet evaporating in the presence of a solid (Fig. 5). Evaporation is nonuniform due to the temperature gradient established along the droplet surface as predicted by the heat transfer and diffusion model from the previous section. The flow in moist air around the droplet generated by the evaporation will be described using the Stokes flow approximation. Even though air viscosity is relatively low, typical values of air flow Reynolds numbers for microscale droplets of interest here are well below unity. For example, in the experimental configuration of Zaitsev *et al.* [13] the Reynolds numbers for the gas phase flow are estimated to be below 0.1.

The discussion of the vapor diffusion model in the previous section suggests a natural choice of the Stefan flow velocity scale

$$V^* = \frac{D\rho_{\mathrm{sat}}}{\rho R}. \tag{20}$$

The Stokes stream function ψ, scaled by R^2V^*, is introduced so that the scaled velocity components are expressed by

$$(u_\xi, u_\eta) = \frac{(\cosh\xi - \cos\eta)^2}{\sinh^2\alpha\,\sin\eta}\left(\frac{\partial\psi}{\partial\eta}, -\frac{\partial\psi}{\partial\xi}\right). \tag{21}$$

The equation of continuity is then satisfied automatically. The momentum equations can be reformulated in terms of the stream function, leading to

$$E^4\psi = 0, \tag{22}$$

where the operator E^2 for axisymmetric flow is defined by

$$E^2 = \frac{\sin\eta(\cosh\xi - \cos\eta)}{\sinh^2\alpha}\left[\frac{\partial}{\partial\xi}\left(\frac{\cosh\xi - \cos\eta}{\sin\eta}\frac{\partial}{\partial\xi}\right) + \frac{\partial}{\partial\eta}\left(\frac{\cosh\xi - \cos\eta}{\sin\eta}\frac{\partial}{\partial\eta}\right)\right]. \tag{23}$$

The standard no-penetration condition ($u_\xi = 0$) implies that the Stokes stream function is equal to a constant value, which can be denoted by ψ_0, along the solid boundary. Since ψ is defined up to an arbitrary constant, we choose $\psi_0 = 0$. Then, the no-penetration and no-slip ($u_\eta = 0$) conditions

are expressed as

$$\psi|_{\xi=0} = 0, \qquad \left.\frac{\partial \psi}{\partial \xi}\right|_{\xi=0} = 0. \tag{24}$$

At the droplet surface, we specify instantaneous evaporation velocity, assumed to be varying linearly in the direction of the imposed temperature gradient, leading to

$$\left.\frac{(\cosh\alpha - \cos\eta)^2}{\sinh^2\alpha\,\sin\eta}\,\frac{\partial \psi}{\partial \eta}\right|_{\xi=\alpha} = -V_0 + V_1(z-h). \tag{25}$$

Here we use a linear approximation for the evaporation velocity as a function of vertical coordinate since evaporative flux variation can be accurately approximated by a linear function, as illustrated by, e.g., the dashed line in Fig. 4. For each fluid flow solution reported, we first solved the corresponding thermal and diffusion problems as formulated in Sec. II to determine V_0 (equal to $-\partial c/\partial n$ at $z = h$) and V_1. Integrating Eq. (25) in η gives

$$\psi|_{\xi=\alpha} = \frac{V\,\sinh^2\alpha}{\cosh\alpha - \cos\eta} - \frac{\frac{1}{2}V_1\sinh^4\alpha}{(\cosh\alpha - \cos\eta)^2} + A'\sinh^2\alpha. \tag{26}$$

Here $V \equiv V_0 + V_1 h$ and the integration constant, A', is determined from the condition that ψ is constant on the symmetry line (where $u_\eta = 0$), leading to

$$A' = -\frac{V + \frac{1}{2}V_1(1-\cosh\alpha)}{1+\cosh\alpha}. \tag{27}$$

Finally, motivated by the much larger viscosity of the liquid compared to air, we impose the no-slip condition at the free surface,

$$\left.\frac{\partial \psi}{\partial \xi}\right|_{\xi=\alpha} = 0, \tag{28}$$

but more detailed discussion of alternative conditions can be found below in Sec. VI. Substantial reduction in mobility of air-water interfaces in small-scale systems is a well-documented effect, e.g., in studies of film drainage [32].

Evaporation at the liquid surface implies that the droplet radius and thus the value of α are changing, making the flow unsteady. We assume the evaporation to be sufficiently slow so that a quasisteady approximation can be used, i.e., that the flow patterns at any moment in time are well described by the solution of the steady-state Stokes flow problem corresponding to the droplet radius at that time.

IV. FLOW PATTERNS

The general solution of Eq. (22) can be written as an expansion of the Stokes stream function in Gegenbauer polynomials of index $-1/2$ [18,21,22],

$$\psi = (\cosh\xi - \cos\eta)^{-3/2}\sum_{n=-1}^{\infty} W_n(\xi)\,C_{n+1}^{-1/2}(\cos\eta). \tag{29}$$

Following Stimson and Jeffery [18], the coefficients of the expansion are often expressed as

$$W_n(\xi) = A_{0n}\cosh n_-\xi + B_{0n}\sinh n_-\xi + C_{0n}\cosh n_+\xi + D_{0n}\sinh n_+\xi, \tag{30}$$

with $n_- = n - 1/2$, $n_+ = n + 3/2$. However, in the present study we use equivalent expressions suggested by Oguz *et al.* [22],

$$W_n(\xi) = \bar{A}_n \frac{\sinh n_-(\alpha - \xi)}{\sinh n_-\alpha} + \bar{B}_n \frac{\sinh n_-\xi}{\sinh n_-\alpha} + \bar{C}_n \left(\frac{\sinh n_-(\alpha - \xi)}{\sinh n_-\alpha} - \frac{\sinh n_+(\alpha - \xi)}{\sinh n_+\alpha} \right) + \bar{D}_n \left(\frac{\sinh n_-\xi}{\sinh n_-\alpha} - \frac{\sinh n_+\xi}{\sinh n_+\alpha} \right), \quad n \geqslant 1, \tag{31}$$

with the coefficients $\bar{A}_n$, $\bar{B}_n$, $\bar{C}_n$, and $\bar{D}_n$ to be determined from the boundary conditions. Furthermore, the conditions of axial symmetry allow one to express W_0 and W_{-1} in terms of only two constants [21], denoted by A and B, so that

$$W_{-1}(\xi) = A\left(\cosh\frac{3\xi}{2} + 3\cosh\frac{\xi}{2} \right) + B\left(\sinh\frac{3\xi}{2} - 3\sinh\frac{\xi}{2} \right), \tag{32}$$

$$W_0(\xi) = A\left(\cosh\frac{3\xi}{2} + 3\cosh\frac{\xi}{2} \right) - B\left(\sinh\frac{3\xi}{2} - 3\sinh\frac{\xi}{2} \right). \tag{33}$$

The boundary conditions at the solid given by Eq. (24) can now be expressed as conditions for W_n and their derivatives,

$$W_n(0) = 0, \tag{34}$$

$$W_n'(0) = 0. \tag{35}$$

At the droplet surface, Eqs. (26) and (28) lead to the conditions

$$W_n(\alpha) = \frac{\sinh^2\alpha}{\sqrt{2}} \left[\frac{3A'}{4} \left(\frac{e^{-\alpha n_+}}{n_+} - \frac{e^{-\alpha n_-}}{n_-} \right) + \left[V + V_1 \left(n + \frac{1}{2} \right) \sinh\alpha \right] e^{-\alpha(n+1/2)} \right], \tag{36}$$

$$W_n'(\alpha) = \frac{3\sinh^3\alpha}{2\sqrt{2}} e^{-\alpha(n+1/2)} \left\{ A' - \frac{(2n+1)V}{\sinh\alpha} - V_1 \left[\left(n + \frac{1}{2} \right) \cosh\alpha + \left(n + \frac{1}{2} \right)^2 \sinh\alpha \right] \right\}. \tag{37}$$

The advantage of using the form of the solution given by (31) instead of (30) is that the conditions (34) and (36) immediately give formulas for two sets of coefficients,

$$\bar{A}_n = 0, \quad \bar{B}_n = W_n(\alpha). \tag{38}$$

The two remaining boundary conditions can then be used to find $\bar{C}_n$ and $\bar{D}_n$, as shown in the Appendix which also outlines the calculation of the coefficients A and B in Eqs. (32) and (33). The description of the viscous flow around the evaporating droplet is now complete. To summarize, the Stokes stream function is represented analytically by Eq. (29). The functions $W_n(\xi)$ are defined by Eqs. (31)–(33) with the coefficients from (38), (A4), (A5), and (A7).

To illustrate the moist air flow patterns around evaporating droplets in situations relevant for experimental study of Zaitsev *et al.* [13], the following solution procedure was adopted. We start by evaluating the key parameters of the thermal problem from Sec. II at the experimentally measured value of the heater temperature. For example, at $T_H = 85\,^\circ\mathrm{C}$ we get parameter values listed in the caption of Fig. 4; note that c_∞ is estimated from the droplet evaporation rate found based on the experimentally measured radius as a function of time, $R(t)$. The full thermal problem with the nonlinear version of the interfacial energy balance, Eq. (8), is then solved as outlined in Sec. II, leading to the scaled evaporative flux profiles such as the one illustrated by the solid line in Fig. 4. The linearized version of the profile (dashed line in the same figure) is then used to determine the input parameters V_0 and V_1 for the flow problem.

The contour plots of the Stokes stream function found from (29), truncated at $n = 10$, are shown in Fig. 6. The plots represent two different values of nondimensional height $h = h^*/R$ corresponding

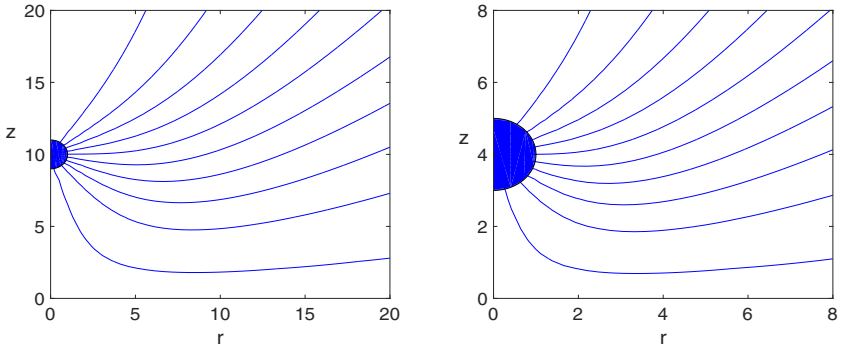

FIG. 6. Flow patterns for evaporating droplet of radius $R = 5$ μm at different heights based on the analytical solution for the Stokes stream function in bipolar coordinates. Scaled levitation heights are $h = 10$ (left) and $h = 4$ (right). Cylindrical coordinates are scaled by the droplet radius.

to two distinct configurations, both encountered in experiments: a small droplet far away from the solid surface and a larger droplet evaporating closer to the solid, i.e., at a distance comparable to its radius. For both cases, the lines under the droplet are bent significantly due to the presence of the solid which cannot be penetrated by the fluid. For the larger h, the lines remain straight near the droplet surface—an indication that flow is nearly spherically symmetric there and only weakly disturbed by the presence of the solid surface far below. For the smaller scaled height, bending starts close to the droplet surface, which is consistent with flow away from the symmetry line in the gas confined between the droplet and the solid. Such flow can be expected to compensate for mass transfer from the evaporating droplets, a situation qualitatively similar to the one seen in the classical studies of the Leidenfrost phenomenon [8].

While our analytical solution for the Stokes stream function is an infinite series, the functions $W_n(\xi)$ in Eq. (29) decay rapidly as n is increased for all values of ξ, so in practice only a few terms in the series are needed to obtain very accurate solutions. In order to illustrate this point, we studied the error in representation of the boundary conditions characterized by the norm of the difference between the truncated series with N terms and the specified boundary values of ψ. Since the boundary conditions at the solid boundary are satisfied exactly due to the way our solution is constructed, we focus on the boundary conditions at the droplet surface. Specifically, we define the norm

$$E_N = \left[\int_0^\pi (\psi_N - \psi_B)^2 d\eta\right]^{1/2}, \tag{39}$$

where ψ_N is the solution at $\xi = \alpha$ given by Eq. (29) but with summation only up to $n = N$ instead of $n = \infty$ and ψ_B is the value of the Stokes stream function at the droplet surface according to Eq. (26). As a measure of relative accuracy of the approximation, we use the scaled quantity $\tilde{E}_N = E_N/\psi_{B\max}$, where $\psi_{B\max}$ is the maximum value of ψ at the droplet surface. Figure 7 shows that $\tilde{E}_N$ decays rapidly as N is increased, indicating that keeping only the first few terms in the expansion is sufficient for obtaining very accurate results. Remarkably, even at $N = 2$, the relative error is already on the order of 10^{-3}. Small values of $\tilde{E}_N$ seen in Fig. 7 together with similar results for ψ_ξ on the boundary (not shown) provide a verification that our analytical solution is indeed correct. Note that the solution given by Eq. (29) satisfies Eq. (22) exactly by construction.

As the droplet size decreases in the configuration of Fig. 5, it is natural to expect the flow pattern to resemble that for a point source near a wall. The inviscid counterpart of this problem is a classical example of the method of images: a source of strength Q at $z^* = h^*$ and an image source of the same strength placed at $z^* = -h^*$ generate the same flow pattern in the physical domain as the source and a solid wall, with the no-penetration condition satisfied everywhere along $z^* = 0$. Remarkably,

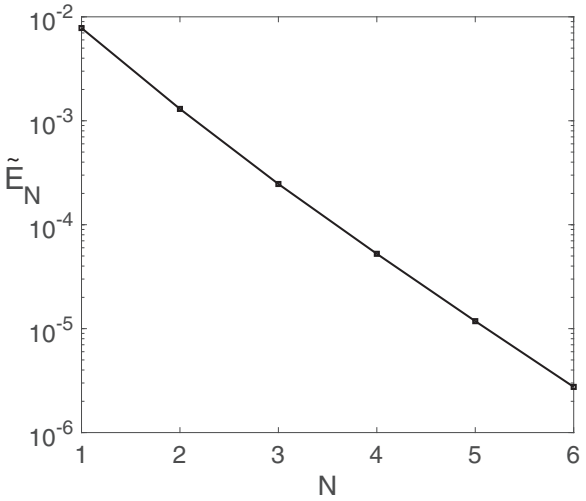

FIG. 7. Scaled error norm of the representation of the stream function with the first N terms in the series expansion shown as a function of the number of terms for $h = 2$.

similar ideas can be applied to the Stokes flow except that three singularities have to be placed simultaneously at the location $z^* = -h^*$ to ensure that not only the no-penetration but also the no-slip condition is satisfied at $z^* = 0$. As shown by Blake and Chwang [33], these singularities are a source, a Stokeslet doublet, and a potential dipole, leading to the velocity field

$$u_i = \frac{Q}{4\pi}\left[\frac{x_i - x_{0i}}{|\mathbf{x}-\mathbf{x}_0|^3} - \frac{x_i}{|\mathbf{x}|^3} + \frac{6x_i x_3^2}{|\mathbf{x}|^5} + 2h^*\left(\frac{\delta_{i3}}{|\mathbf{x}|^3} - \frac{3x_i x_3}{|\mathbf{x}|^5}\right)\right], \quad i = 1, 2, 3. \tag{40}$$

Here we use Cartesian coordinates with the origin at the location of the image, with $\mathbf{x}$ being the position vector and $\mathbf{x}_0$ the value of the position vector corresponding to the location of the actual physical source. The x_3 axis is in the vertical direction and δ denotes the Kronecker delta. The flow pattern defined by (40) can now be compared to the predictions of our model, i.e., the velocity components found from the Stokes stream function based on Eq. (21). Figure 8 illustrates a typical comparison for scaled radial and vertical velocity components plotted as functions of radial coordinate in the plane corresponding to $z = (h-1)/2$, i.e., halfway between the bottom of the droplet and the solid surface for two different levitation heights. Even though strictly speaking the method of images is valid in the limit of infinitely small droplet radius, i.e., $h \to \infty$, it clearly provides rather accurate velocity predictions even at the moderately large values of h, e.g., $h = 10$ shown in the top plots in Fig. 8. However, for smaller nondimensional levitation heights, the differences in the predictions of the model become significant, as seen in the bottom two images in Fig. 8. In particular, the method of images tends to underestimate the velocity under the droplet.

The method of images provides a simple physical interpretation of the experimentally observed ability of evaporating microscale droplets to levitate at temperatures well below the Leidenfrost point [13]. According to Eq. (40), the flow generated by the image has the upward velocity at the location of the droplet given by

$$U = \frac{3Q}{16\pi h^{*2}}. \tag{41}$$

Thus the droplet ends up being suspended in this upward flow and, for sufficiently small weight and strong evaporation, it will be able to levitate. More detailed discussion of the levitation conditions is provided below.

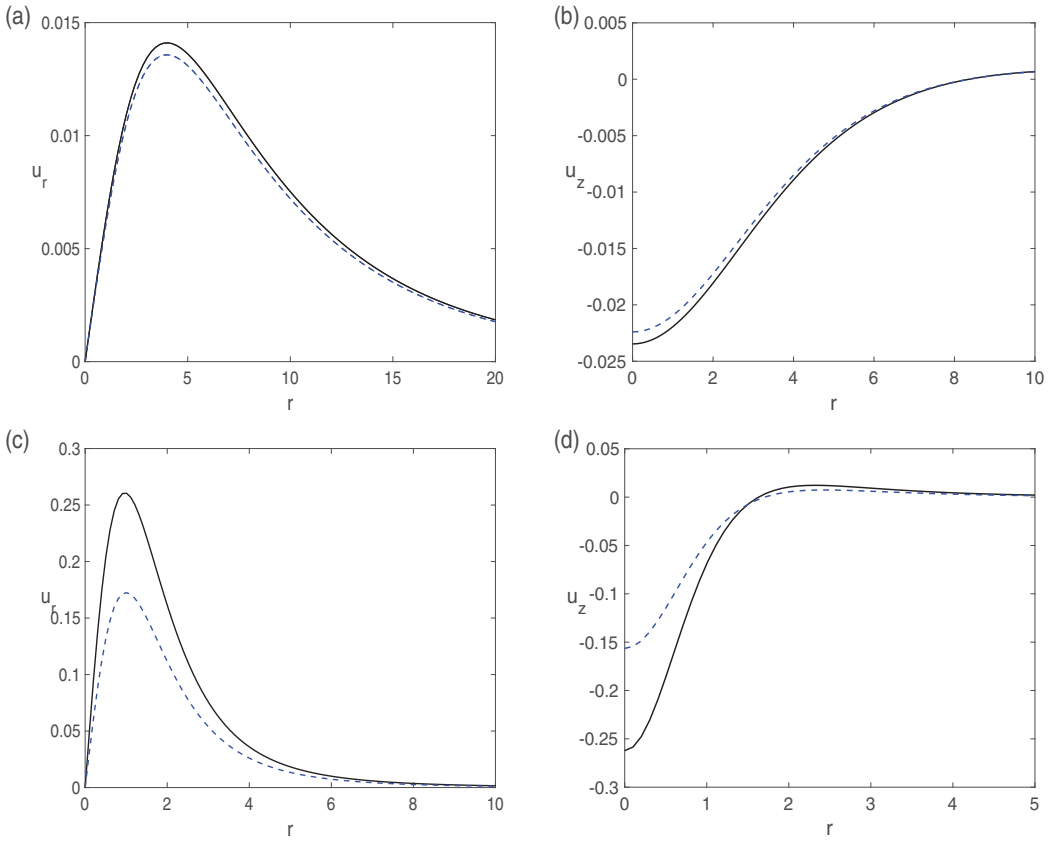

FIG. 8. Profiles of nondimensional radial (a), (c) and vertical (b), (d) velocities at $z = (h-1)/2$ corresponding to $h = 10$ (top plots) and $h = 2$ (bottom plots). Solid lines represent the model predictions based on (29), while dashed lines are obtained from the method of images, Eq. (40).

V. STOKES FORCE

Let us now turn to the calculation of the force acting on the droplet from the flow around it. This force is the key quantity needed for determination of levitation conditions as well as describing motion of evaporating droplets near interfaces in other applications such as spray cooling. For the Stokes stream function represented by Eq. (30), the general formula for the dimensional force has been first derived by Stimson and Jeffery [18]. While their geometric configuration is different, the result for the force was presented in terms of the coefficients of the general solution given by Eqs. (29) and (30) and is therefore applicable to our configuration as well. With the alternative form of the solution given by (31)–(33), their formula can be expressed as

$$F = 2\sqrt{2}\pi \frac{\mu R V^*}{\sinh\alpha}\left[4B - \sum_{n=1}^{\infty}\left(\frac{\bar{B}_n + \bar{D}_n - (\bar{A}_n + \bar{C}_n)\cosh n_-\alpha}{\sinh n_-\alpha} + \frac{\bar{C}_n \cosh n_+\alpha - \bar{D}_n}{\sinh n_+\alpha}\right)\right], \quad (42)$$

where μ is the moist air viscosity. For small droplets levitating far above the heater (large h), the expression for the force is expected to be equivalent to the classical Stokes law,

$$F_0 = 6\pi\mu R U, \quad (43)$$

with U found from Eq. (41). In order to illustrate departures from this formula, it is convenient to define the nondimensional force $\hat{F} = F/F_0$. This quantity is plotted in Fig. 9 as a function of the

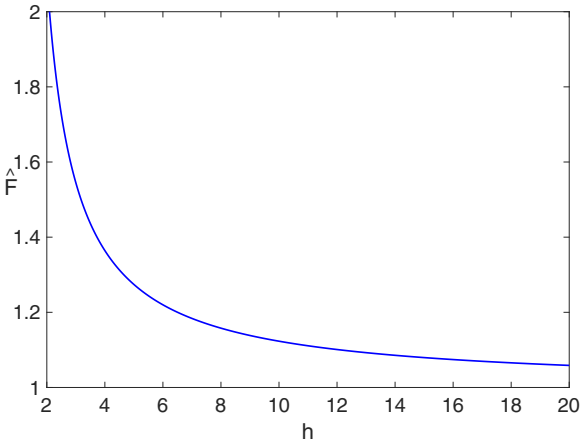

FIG. 9. Vertical force, scaled by F_0 from (43), acting on an isolated evaporating droplet near a solid surface, as a function of the scaled distance between droplet's center and the solid surface, for uniform evaporation velocity at the interface, $V^* = 0.01$ m/s.

scaled levitation height. As expected, $\hat{F}$ approaches unity at large h, i.e., where the method of images is valid. However, as h is decreased, due to either increase in the radius or decrease in distance to the solid, the force becomes significantly larger than expected from (41) and (43). For example, a droplet of radius 2 μm at a distance of 10 μm experiences repulsion force almost 30% greater than predicted if the droplet is treated as a point source. The discrepancy between the predictions of the two models increases dramatically as $h \to 1$, i.e., when the gap between the droplet and the solid becomes vanishingly small. This is not surprising since maintaining viscous flow in the narrow gap requires substantial increase in the pressure under the droplet, leading to sharp increase in the force acting on it, an effect qualitatively similar to strong repulsion of Leidenfrost droplets [8,34] from hot surfaces. There are, however, important quantitative differences since our model focuses on evaporation at much lower temperatures, motivated by experiments conducted for solid surface temperatures in the range of 50–100 °C [13,35], and does not account for interface deformation at the bottom of the droplet.

Let us now vary V_1 to investigate the effect of nonuniform evaporation (due to local temperature gradient near the heater) on the force F. Typical force vs distance curves for two realistic nonzero values of V_1 together with the case of uniform evaporation (dashed line) are shown in Fig. 10 (top). The predictions for all three cases are similar at h below $\sim$2, but deviate strongly for large values of h at which evaporation nonuniformity leads to higher values of the repulsion force. The fact that the force does not decay to zero when the droplet is far away from the solid may appear puzzling, but can be explained by observing that the net momentum lost by the droplet during evaporation with nonzero V_1 is in fact not zero even when no solid is present. This net momentum can assist in droplet levitation and contribute to the takeoff phenomenon seen in several experimental studies of evaporating microscale droplets ([10,11]; see also Supplemental Material from [13]). We note that Fig. 10 (top) shows relative value of the force (scaled by F_0), but the actual force magnitude approaches constant at large h^*. To verify this, we plotted the dimensional force as a function of dimensional height in Fig. 10 (bottom). The asymptotic behavior for the nonzero value of V_1 clearly shows that far away from the solid the force does not decay to zero, in contrast to the case of $V_1 = 0$ when the force is solely due to droplet-solid interaction.

VI. THERMOCAPILLARY STRESSES

The temperature gradient in the gas phase near the heater implies that thermocapillary stresses at the droplet surface may need to be accounted for. Accurate and complete description of the

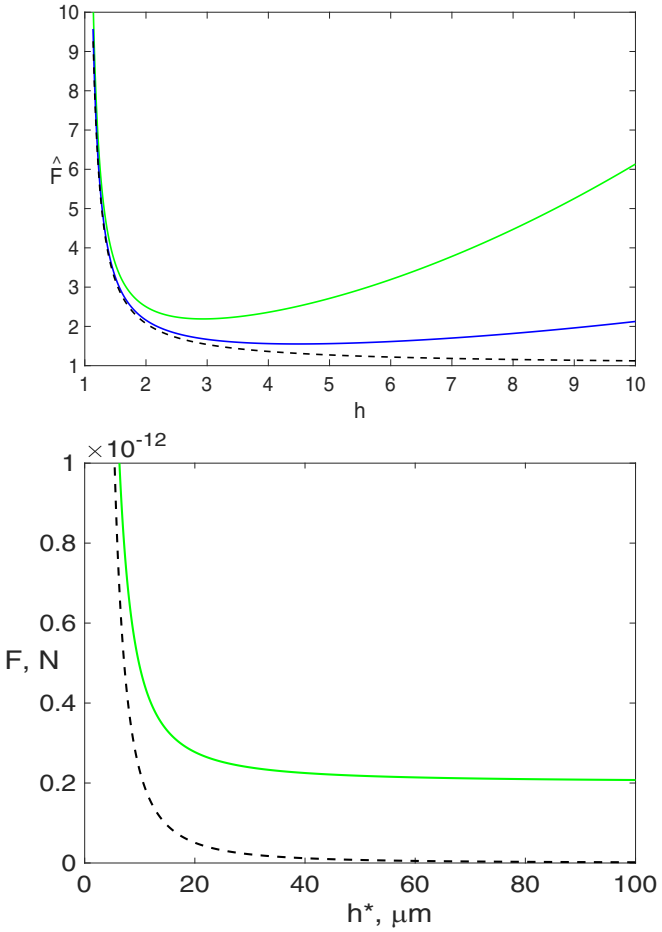

FIG. 10. (Top) Scaled force acting on the droplet ($R = 2\ \mu$m; $V^* = 0.01$ m/s) as predicted by models with different temperature gradients, characterized by different values of V_1: $V_1 = 0.01V_0$ (blue line); $V_1 = 0.05V_0$ (green line). The dashed line corresponds to $V_1 = 0$. (Bottom) For $V_1 = 0.05V_0$, the same result is plotted in dimensional variables, with dashed line showing dimensional force for $V_1 = 0$.

Marangoni effect would require solving coupled equations for viscous flow both inside and outside of the droplet with the shear stress condition incorporating thermocapillary stresses. This type of solution is beyond the scope of the present study. Instead, our objective here is to evaluate the significance of the Marangoni effect using a simple modification of the flow model developed in Sec. III. Specifically, instead of the no-slip condition at the droplet surface we impose the value of the tangential velocity that matches the classical Hadamard-Rybczynski–type solution as applied to a spherical droplet in uniform vertical temperature gradient [36]. In our formulation, this strategy implies replacing the boundary condition (28) with

$$\left.\frac{\partial \psi}{\partial \xi}\right|_{\xi=\alpha} = \frac{v_T \sinh^3\alpha\ \sin^2\eta}{(\cosh\alpha - \cos\eta)^3}, \tag{44}$$

where v_T is the scaled maximum value of the Marangoni-induced velocity at the droplet surface, typically well below unity. Using the series expression from (29), the condition (44) can be

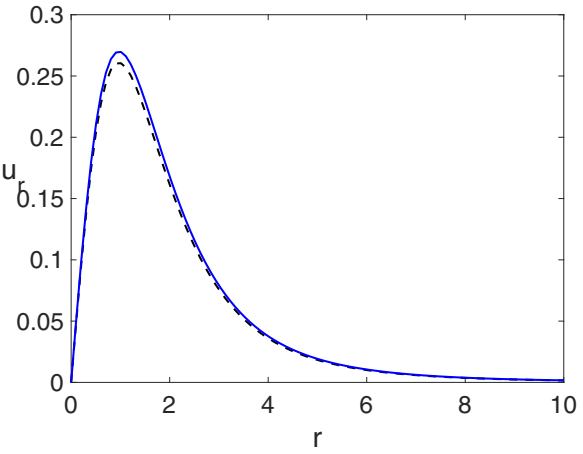

FIG. 11. Comparison of predictions of models with and without thermocapillary effect, with solid line corresponding to $v_T = 0.01$ and dashed line to $v_T = 0$. All results are obtained at $R = 2$ μm, $V_1 = 0$; the plot represents the radial velocity at $z = 1/2$ for $h = 2$.

reformulated in terms of expansion in Gegenbauer polynomials as follows:

$$\frac{2}{3\,\sinh^3\alpha}\sum_{n=-1}^{\infty} W_n'(\alpha)\,C_{n+1}^{-1/2}(\cos\eta) = (\cosh\alpha-\cos\eta)^{1/2}A' + \frac{V}{(\cosh\alpha-\cos\eta)^{1/2}} - \frac{V_1\sinh^2\alpha}{2(\cosh\alpha-\cos\eta)^{3/2}} + \frac{2v_T}{3}\frac{\sin^2\eta}{(\cosh\alpha-\cos\eta)^{3/2}}. \quad (45)$$

One could now proceed to formulating the condition for $W_n'(\alpha)$ analogous to Eq. (37) and then solving the problem for the stream function. However, there is a simple observation which allows one to drastically simplify the calculation. The right-hand side of Eq. (45) can be made identical to the previously discussed case of $v_T = 0$ by the following transformation of the key parameters:

$$A' \to A' - \tfrac{2}{3}v_T, \quad V \to V + \tfrac{4}{3}v_T\cosh\alpha, \quad V_1 \to V_1 + \tfrac{4}{3}v_T. \quad (46)$$

Both flow patterns and force acting on the droplet can then be determined from the previously derived results. Figure 11 shows typical radial velocity profiles halfway between the bottom of the droplet and the solid with and without the thermocapillary effect taken into account. Slight increase in the radial velocity is seen for nonzero v_T (solid line), consistent with the linearity of Stokes flow suggesting superposition of the additional thermocapillary contribution and the flow caused by evaporation at the liquid surface.

The action of thermocapillary stresses pushing moist air away from the axis of symmetry, where the drop surface temperature is the highest, suggests that the force acting on the droplet should be reduced for nonzero v_T due to reduction of pressure under the droplet. We checked that this is indeed the case, but the effect is rather small under realistic conditions, mostly due to the fact that droplet surface is close to isothermal even under the imposed temperature gradient, as was demonstrated in our solution of the heat transfer problem above. We also note that in experiments water is typically used and so potential surface contamination may affect the surface tension variation.

VII. COMPARISON WITH EXPERIMENTS

Experimental measurements of the droplet levitation height have been carried out for arrays of evaporating droplets formed over a dry patch in a thin layer of water on a metal surface, as shown in

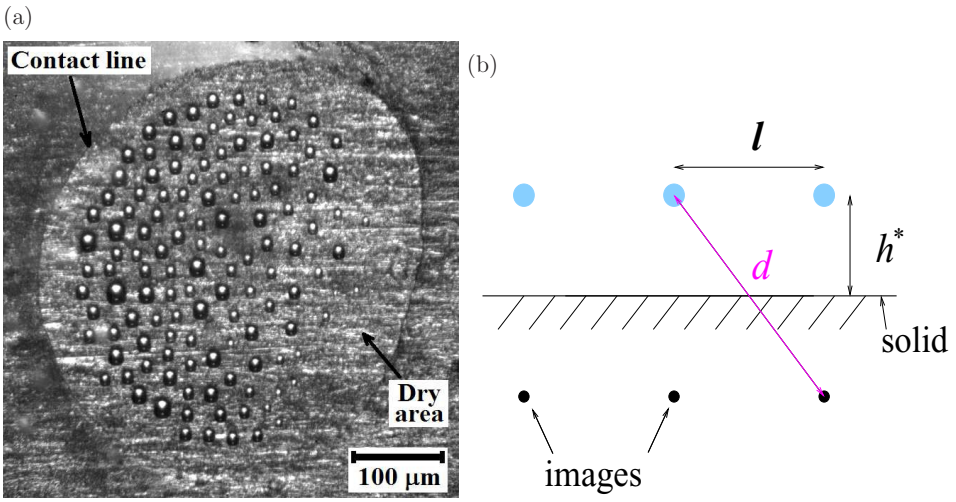

FIG. 12. (a) Photo of an array of droplets levitating over a dry patch at 85 °C, from [13]. (b) Sketch illustrating the calculation of correction factor due to interaction of droplet with images.

the top-view picture in Fig. 12(a). The droplets were formed by condensation of vapor over the liquid layer and ended up levitating in the dry-patch region after flying over the contact line, as described in detail in several recent studies [12,13,35,37]. Levitation height was recorded and compared to the predictions of the model representing droplets as point sources by Zaitsev *et al.* [13]. They suggested that a correction factor should be introduced in the expression for the upward force to account for the effect of flow generated by neighboring droplets and their images. The sketch in Fig. 12(b) illustrates the correction factor estimate using a two-dimensional version of the problem in which all droplets are on a straight line, separated by the distance l from each other. The droplet in the middle is at a distance $d = \sqrt{l^2 + 4h^{*2}}$ from the image of its neighbor on the right, and the flow generated by that image has a vertical component calculated from Eq. (40) to be $6Qh^3/(\pi d^5)$. A similar argument can be made for the three-dimensional case except that the velocity correction has to be multiplied by 6—the typical number of nearest neighbors in the two-dimensional array. Based on images such as the one shown in Fig. 12(a), we find that $l \sim 2h^*$ gives a reasonable estimate of interdroplet distance, leading to the final result for the correction factor to the Stokes drag force:

$$\beta_F = 1 + \frac{3}{2\sqrt{2}}. \tag{47}$$

Zaitsev *et al.* [13] used similar arguments although they ended up with a larger value of β_F (corresponding to β^2 in their notation), as appropriate for larger levitation heights. Estimating the upward force from (43) with that correction factor, they predicted levitation height as a function of droplet radius and compared it with the experimental data. The agreement was good for large levitation heights ($h \sim 10$), thus providing important early support for the hypothesis of the levitation mechanism through the flow generated by the evaporation of the droplet itself rather than other convective flows in the moist air. However, the model did not agree with the experimental data when levitation height was comparable to the radius. The disagreement was not only quantitative but qualitative, as theory predicted the dimensional levitation height to decrease with the radius, while experimental data showed gradual increase in this quantity.

Let us now discuss how the model formulated in Sec. III compares with the experimental data. We assume that the quasisteady approximation formulated there is acceptable for evaluating the upward force acting on the droplet and use the balance between Stokes force and droplet weight

written in the form

$$\tfrac{4}{3}\pi R^3 \rho_l g = \beta_F F. \tag{48}$$

Here ρ_l is liquid density, g is acceleration of gravity, F is determined from (42), the value of evaporation velocity is found from the rate of change of the radius based on experimental measurements, and the correction factor is given by Eq. (47). Strictly speaking, the argument used in deriving Eq. (47) is valid only for point sources, but we use the same value of the correction factor for finite-size droplets, assuming that inaccuracies in β_F introduce errors comparable to other effects we are neglecting in this section by setting V_1 and v_T to zero, e.g., neglecting spatial nonuniformity of evaporative flux and thermocapillary stresses. Since local temperature gradients were not measured in experiments, an attempt to include these effect would introduce additional fitting parameters which would have to be adjusted during comparison between experiment and theory. Instead, we focus on the main physical effect here, the repulsive interaction between droplets and the solid surface, and neglect smaller secondary effects.

The right-hand side of Eq. (48) is a function of h, so it gives an implicit equation for levitation height, solved using `fzero` subroutine in MATLAB. The comparison between the predictions of our model and the experiments is illustrated in Fig. 13. Levitation height (scaled by R) is shown as a function of the nondimensional droplet radius defined by

$$\hat{R} = R\left(\frac{\mu V^*}{\rho_l g}\right)^{-1/2} \tag{49}$$

for four different droplets, represented by different marker types, at the same experimental conditions corresponding to the metal substrate temperature of 85 °C, as measured by thermocouples. First, we note that the vast majority of experimental data seen in Fig. 13 (top) lies either on or very close to the theoretical curve (solid line). There is some disagreement at small $\hat{R}$, which we believe to be due to a combination of three factors. First, the estimate of the coefficient β_F from Eq. (47) becomes increasingly inaccurate since the interdroplet distance is not changing significantly for smaller droplets while levitation height increases (note that a larger value of $\beta_F = 3.4$ was used in Zaitsev *et al.* [13] for small droplets, which, however, is no longer accurate for larger droplets of interest here). Second, the accuracy of experimental measurement is reduced for droplets of small size since the optical resolution is limited, which also explains the significant experimental scatter seen in the plot. Third, as the droplet height increases, convective flow in the gas not related to the presence of droplets is likely to contribute more to the balance of forces acting on the droplet. Experiment and theory also diverge slightly at larger $\hat{R}$. To better illustrate this region, we plot the data and the solid line corresponding to the theory in log-log coordinates over a subset of the values of $\hat{R}$ in Fig. 13 (bottom). The theory tends to slightly overpredict the levitation height at larger $\hat{R}$, although it is clearly much more accurate than the approximate model based on the method of images, shown by the dashed line for comparison. It is also important to note that neglecting the nonuniformity of evaporation rate and thermocapillary stresses can contribute to the discrepancies at smaller levitation heights. In particular, thermocapillary stresses tend to reduce the upward force acting on the droplet, and thus can lead to lower levitation height than predicted by the models without thermocapillarity. However, without direct measurements of the temperature gradient near the heater it remains unclear if the only reason for discrepancy is the flow induced by thermocapillary stresses.

VIII. CONCLUSIONS

We developed an analytical model of flow around an evaporating spherical droplet near a heated solid surface based on solving the equation for the Stokes stream function in bipolar coordinates. The model allows us to calculate the force acting on the droplet and determine levitation height as a function of evaporation conditions. Previous modeling efforts treated droplets as point sources and did not match the experimental data except for very small values of the radius. We show that

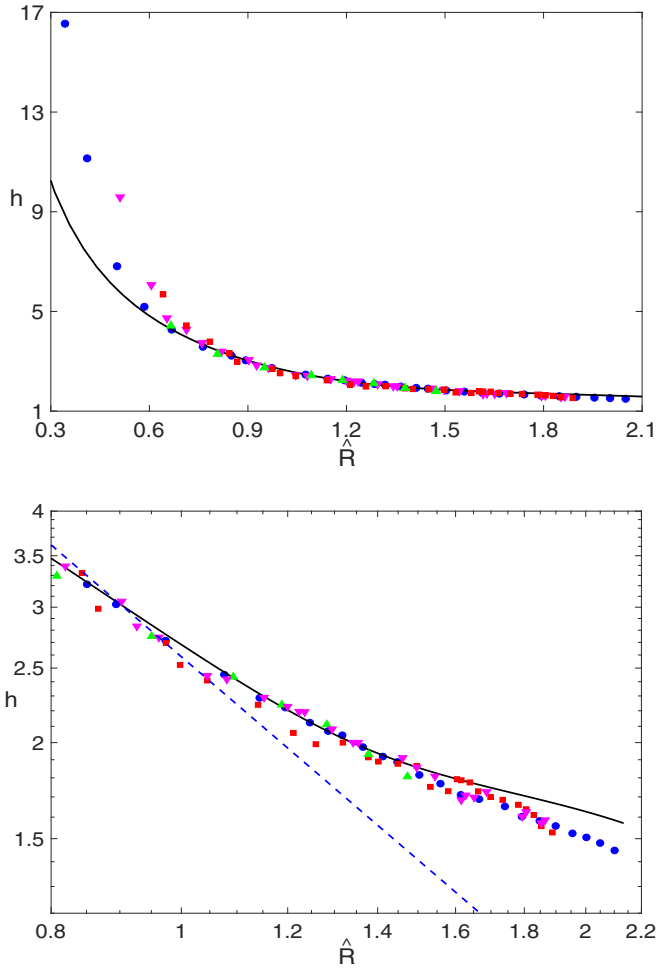

FIG. 13. (Top) Comparison between the experimental (markers, representing four different droplets under the same experimental conditions) and theoretical results (solid line, $V_1 = v_T = 0$) for scaled levitation height. (Bottom) The subset of the same results (for $\hat{R} \geqslant 0.8$) plotted in log-log coordinates, with the dashed line corresponding to the model representing droplets as point sources.

our model provides a much better agreement with the experimental results from studies of arrays of droplets levitating over heated dry solid surfaces at temperatures below 100 °C. Possible reasons for remaining discrepancies between experiment and theory are identified, including convective air flow not related to the presence of the droplet and thermocapillary stresses pushing the moist air out of the gap between the droplet and the heater.

Our approach provides a natural framework for incorporating thermocapillary stresses into the models of evaporating droplets. In the present study, we only took an initial step in that direction by considering prescribed tangential velocity at the droplet surface based on classical solutions for viscous flow inside and outside of a droplet placed in a temperature gradient, as derived by Young *et al.* [36]. While generally not a very strong effect, it can still affect levitation conditions, especially if the repulsive hydrodynamic interaction with the solid is weak. The Marangoni effect is also competing with the force due to nonuniform evaporation, leading to net momentum loss pushing the droplet in the upward vertical direction. To evaluate the relative importance of these

effects, we developed an analytical model of heat transfer both inside and outside of the droplet coupled with vapor diffusion through air. The model shows that the vertical temperature gradient along the droplet surface is much smaller than the temperature gradient in air away from the droplet. Evaporation is stronger at the bottom of the droplet than at the top but is found to unexpectedly weaken as the droplet gets closer to the wall, an effect explained by the geometric confinement that impedes vapor diffusion away from the free surface.

We used the measured values of the rate of decrease of the radius in our comparison between theory and experiment. It is interesting to note that estimates based on the classical Maxwell-type models of diffusive evaporation predict significantly faster evaporation rate if the humidity far away from the droplet is assumed to be at the value corresponding to ambient air. Observed evaporation rates suggest that air around the droplet has high vapor concentration, most likely due to intensive evaporation from the liquid layer surrounding the dry patch [12]. Nonuniformity of vapor concentration around the droplets can also explain the deviations from the classical D^2 law predicted by Maxwell-type models of evaporating droplets in the experimental data [35].

It is seen in the experimental photos such as Fig. 12(a) that levitating droplets tend to form ordered arrays. The quantitative description of this self-organization is beyond the scope of the present paper, but we believe that the method based on bispherical coordinates discussed in the present work will be applicable to studies of self-organization as well since it allows one to determine forces of pairwise interaction between droplets.

ACKNOWLEDGMENTS

The work was supported by the Russian Science Foundation (Grant No.18-19-00538). We thank D. P. Kirichenko for valuable discussions and for sharing experimental data with us.

APPENDIX

For the heat transfer model of Sec. II, the coefficients A_n satisfy

$$
\begin{aligned}
&-n(k\,\cosh n_-\alpha+\sinh n_-\alpha+E^{-1}\gamma\,\tanh n_-\alpha\,\sinh n_-\alpha)A_{n-1}\\
&+[(k-1)\sinh\alpha\,\sinh\bar{n}\alpha+2\bar{n}\,\cosh\alpha(k\,\cosh\bar{n}\alpha+\sinh\bar{n}\alpha)\\
&+E^{-1}\gamma(\sinh\alpha+2\bar{n}\,\cosh\alpha\,\tanh\bar{n}\alpha)\sinh\bar{n}\alpha\big]A_n\\
&-(n+1)(k\,\cosh n_+\alpha+\sinh n_+\alpha+E^{-1}\gamma\,\tanh n_+\alpha\,\sinh n_+\alpha)A_{n+1}\\
&=\sqrt{2}\,e^{-\alpha\bar{n}}[\sinh\alpha-2\bar{n}\,\cosh\alpha+G\,\sinh\alpha\{2k\,\cosh\alpha-2\bar{n}[(2k+1)\sinh\alpha-2\bar{n}\,\cosh\alpha]\}\\
&-E^{-1}(\sinh\alpha+2\bar{n}\,\cosh\alpha\,\tanh\bar{n}\alpha)(1-c_\infty-2\gamma G\,\sinh\alpha)]\\
&+\sqrt{2}n\,e^{-n_-\alpha}[1-2n_-G\,\sinh\alpha+E^{-1}\tanh n_-\alpha(1-c_\infty-2\gamma n_-G\,\sinh\alpha)]\\
&+\sqrt{2}(n+1)e^{-n_+\alpha}[1-2n_+G\,\sinh\alpha+E^{-1}\tanh n_+\alpha(1-c_\infty-2\gamma n_+G\,\sinh\alpha)].
\end{aligned}
\tag{A1}
$$

Here $\bar{n}=n+1/2$, $n_+=n+3/2$, and $n_-=n-1/2$.

For the flow model of Sec. III, the conditions given by Eqs. (24) and (28) lead to

$$
(n_+\coth n_+\alpha-n_-\coth n_-\alpha)\bar{C}_n+(n_-\mathrm{csch}\,n_-\alpha-n_+\mathrm{csch}\,n_+\alpha)\bar{D}_n=-n_-W_n(\alpha)\mathrm{csch}\,n_-\alpha,
\tag{A2}
$$

$$
\begin{aligned}
&(n_+\mathrm{csch}\,n_+\alpha-n_-\mathrm{csch}\,n_-\alpha)\bar{C}_n-(n_+\coth n_+\alpha-n_-\coth n_-\alpha)\bar{D}_n\\
&\quad=-n_-W_n(\alpha)\coth n_-\alpha+W_n'(\alpha).
\end{aligned}
\tag{A3}
$$

The solution of this linear system is

$$\bar{C}_n = \Delta_n^{-1}[n_- n_+ W_n(\alpha)(\cosh n_+\alpha - \cosh n_-\alpha) + W_n'(\alpha)(n_+ \sinh n_-\alpha - n_- \sinh n_+\alpha)], \tag{A4}$$

$$\bar{D}_n = \Delta_n^{-1}\{n_- W_n(\alpha)[n_- \sinh n_-\alpha \sinh n_+\alpha + n_+(1 - \cosh n_+\alpha \cosh n_-\alpha)] + W_n'(\alpha)(n_+ \cosh n_+\alpha \sinh n_-\alpha - n_- \cosh n_-\alpha \sinh n_+\alpha)\}, \tag{A5}$$

$$\Delta_n = 2n_- n_+(\cosh n_+\alpha \cosh n_-\alpha - 1) - (n_-^2 + n_+^2)\sinh n_+\alpha \sinh n_-\alpha. \tag{A6}$$

Let us now discuss the procedure for finding the coefficients A and B appearing in Eqs. (32) and (33). Since the stream function is zero at $\xi = 0$ and $\eta = \pi$, the value of A is immediately found to be zero. Application of the condition (26) at $\eta = 0$ leads to the determination of the value of B. To summarize the results, we write

$$A = 0, \quad B = \frac{2\sqrt{2}\,\sinh^3(\alpha/2)(V - V_1\cosh\alpha)}{\sinh\frac{3\alpha}{2} - 3\sinh\frac{\alpha}{2}}. \tag{A7}$$

[1] J. Kim, Spray cooling heat transfer: The state of the art, Int. J. Heat Fluid Flow **28**, 753 (2007).

[2] W. Sirignano, *Fluid Dynamics and Transport of Droplets and Sprays*, 2nd ed. (Cambridge University Press, Cambridge, UK, 2014).

[3] C. Kleinstreuer and Z. Zhang, Airflow and particle transport in the human respiratory system, Annu. Rev. Fluid Mech. **42**, 301 (2010).

[4] J. C. Maxwell, Diffusion, collected scientific papers, *Encyclopedia Britannica* (Cambridge University Press, Cambridge, 1890), Vol. II, pp. 625–646.

[5] S. Sazhin, *Droplets and Sprays* (Springer-Verlag, London, 2014).

[6] J. Stefan, Versuche uber die verdampfung, Sitz. k. Akad. Wiss. Wien II **65**, 385 (1873).

[7] N. Fuchs, *Evaporation and Droplet Growth in Gaseous Media* (Pergamon, London, 1959).

[8] D. Quéré, Leidenfrost dynamics, Annu. Rev. Fluid Mech. **45**, 197 (2013).

[9] T. Tran, H. J. J. Staat, A. Prosperetti, C. Sun, and D. Lohse, Drop Impact on Superheated Surfaces, Phys. Rev. Lett. **108**, 036101 (2012).

[10] F. Celestini, T. Frisch, and Y. Pomeau, Take Off of Small Leidenfrost Droplets, Phys. Rev. Lett. **109**, 034501 (2012).

[11] S. Lyu, V. Mathai, Y. Wang, B. Sobac, P. Colinet, D. Lohse, and C. Sun, Final fate of a Leidenfrost droplet: Explosion or takeoff, Sci. Adv. **5**, eeav8081 (2019).

[12] O. A. Kabov, D. V. Zaitsev, D. P. Kirichenko, and V. S. Ajaev, Interaction of levitating microdroplets with moist air flow in the contact line region, Nanoscale Microscale Thermophys. Eng. **21**, 60 (2017).

[13] D. V. Zaitsev, D. P. Kirichenko, V. S. Ajaev, and O. A. Kabov, Levitation and Self-Organization of Liquid Microdroplets Over Dry Heated Substrates, Phys. Rev. Lett. **119**, 094503 (2017).

[14] V. S. Ajaev and O. A. Kabov, Levitation and self-organization of droplets, Annu. Rev. Fluid Mech. **53**, 203 (2021).

[15] A. A. Fedorets, Droplet cluster, JETP Lett. **79**, 372 (2004).

[16] A. A. Fedorets, I. Marchuk, and O. Kabov, Role of vapor flow in the mechanism of levitation of a droplet-cluster dissipative structure, Tech. Phys. Lett. **37**, 116 (2011).

[17] V. J. Schaefer, Observations of an early morning cup of coffee, Am. Sci. **59**, 534 (1971).

[18] M. Stimson and G. B. Jeffery, The motion of two spheres in a viscous fluid, Proc. R. Soc. A **111**, 110 (1926).

[19] H. Brenner, The slow motion of a sphere through a viscous fluid towards a plane surface, Chem. Eng. Sci. **16**, 242 (1961).

[20] L. S. Fisher and A. A. Golovin, Motion of a droplet near an evaporating liquid-gas interface, Phys. Fluids **19**, 032101 (2007).

[21] H. N. Oguz and S. S. Sadhal, Growth and collapse of translating compound multiphase drops: Analysis of fluid mechanics and heat transfer, J. Fluid Mech. **179**, 105 (1987).
[22] H. N. Oguz, A. Prosperetti, and D. Antonelli, The hydrodynamic interaction of two slowly evaporating spheres, Phys. Fluids A **1**, 1656 (1989).
[23] G. E. Cossali and S. Tonini, Variable gas density effects on transport from interacting evaporating spherical drops, Int. J. Heat Mass Transf. **127**, 485 (2018).
[24] T. Brzustowski, E. Twardus, S. Wojcicki, and A. Sobiesiak, Interaction of two burning fuel droplets of arbitrary size, AIAA J. **17**, 1234 (1979).
[25] A. Umemura, S. Ogawa, and N. Oshima, Analysis of the interaction between two burning droplets, Combust. Flame **41**, 45 (1981).
[26] S. Zhang and G. Gogos, Film evaporation of a spherical droplet over a hot surface: Fluid mechanics and heat/mass transfer analysis, J. Fluid Mech. **222**, 543 (1991).
[27] P. T. Tsilingiris, Thermophysical and transport properties of humid air at temperature range between 0 and 100 °C, Energy Convers. Manage. **49**, 1098 (2008).
[28] L. R. Glicksman and J. H. Lienhard V, *Modeling and Approximation in Heat Transfer* (Cambridge University Press, Cambridge, UK, 2016).
[29] E. Arinshtein and A. A. Fedorets, Mechanism of energy dissipation in a droplet cluster, JETP Lett. **92**, 658 (2010).
[30] S. S. Sadhal, Heat transport to a slowly growing bubble on a solid surface, Q. J. Mech. Appl. Math. **42**, 477 (1989).
[31] N. N. Lebedev, *Special Functions and their Applications* (Dover, New York, 1972).
[32] R. Manica and D. Y. C. Chan, Drainage of the air-water-quartz film: experiments and theory, Phys. Chem. Chem. Phys. **13**, 1434 (2011).
[33] J. R. Blake and A. T. Chwang, Fundamental singularities of viscous flow, Part I, J. Eng. Math. **8**, 23 (1974).
[34] B. Sobac, A. Rednikov, S. Dorbolo, and P. Colinet, Leidenfrost effect: Accurate drop shape modeling and refined scaling laws, Phys. Rev. E **90**, 053011 (2014).
[35] D. V. Zaitsev, D. P. Kirichenko, A. I. Shatekova, V. S. Ajaev, and O. A. Kabov, Experimental and theoretical studies of ordered arrays of microdroplets levitating over liquid and solid surfaces, Interfac. Phenom. Heat Transfer **6**, 219 (2018).
[36] N. O. Young, J. S. Goldstein, and M. J. Block, The motion of bubbles in a vertical temperature gradient, J. Fluid Mech. **6**, 350 (1959).
[37] O. A. Kabov, D. V. Zaitsev, D. P. Kirichenko, and V. S. Ajaev, Investigation of moist air flow near contact line using microdroplets as tracers, Interfac. Phenom. Heat Transfer **4**, 207 (2016).